

On the question of noise as a resource in quantum computing

J. Montes,^{1,*} F. Borondo,^{2,†} and Gabriel G. Carlo^{3,‡}

¹*Grupo de Sistemas Complejos, ETSIME, Universidad Politécnica de Madrid, Ríos Rosas 21, 28003 Madrid, Spain*

²*Departamento de Química, Universidad Autónoma de Madrid, Cantoblanco, 28049 Madrid, Spain*

³*Comisión Nacional de Energía Atómica, CONICET, Departamento de Física,*

Av. del Libertador 8250, 1429 Buenos Aires, Argentina

(Dated: May 29, 2026)

Noise is usually regarded as the main obstacle to achieving a scalable quantum advantage, but recent evidence in quantum reservoir computing [1] suggests that certain channels can, in appropriate regimes, improve performance by enriching the reservoir's effective dynamics. Motivated by this idea we propose a geometric mechanism to explain how non-unital noise applied together with a universal gate set leads to a faster approach to Haar-like distributions of the final states. We find that noise of this kind induces an effective volume expansion on the manifold of pure states. In order to intuitively understand this we use a minimal 1 qubit model where we take the amplitude damping channel and combine it with a renormalization rule that associates to each resulting mixed state a representative pure state. This composition defines a globally expanding nonlinear map on the space of pure states. We analytically derive the local area expansion factor and identify the global expansion threshold. Finally, we combine amplitude damping with the $G3 = \{H, T, \text{CNOT}\}$ universal gate set to show how the approach to Haar-like behavior is faster in an appropriate parameter region. This leads us to propose noise as a possible resource in future quantum algorithms.

I. INTRODUCTION

Recent advances in programmable quantum processors have placed quantum computing at the center of the debate on computational advantages beyond classical reach. In particular, random circuit sampling experiments and their variants have motivated claims of quantum supremacy on superconducting and photonic platforms [2, 3], as well as theoretical analyses of what such supremacy precisely means and under which assumptions it can be regarded as robust [4]. These demonstrations, however, have been accompanied by controversy and classical (or hybrid) rebuttals that stress-test the boundary between the quantum and the classical in realistic scenarios [5, 6].

In the current era of noisy intermediate-scale quantum (NISQ) devices operations are noisy and coherence is limited, which degrades the execution of algorithms and any potential scalable advantage. As a result, a substantial part of the effort has focused on error correction (and its scalability) and on output error mitigation [7–11]. However, can we identify mechanisms by which noise could help to increase effective quantum randomness?

This question has become especially relevant in quantum learning algorithms that exploit complex dynamics as a resource. A paradigmatic example is quantum reservoir computing (QRC), where a circuit (the reservoir) effectively transforms input information and its observables feed a classical model. There is by now a substantial literature establishing the potential of quantum reservoirs and their processing capabilities [12–19]. In

this context, it has been observed that not all noise is equivalent: whereas unital channels such as depolarizing or dephasing degrade performance, non-unital channels (in particular, *amplitude damping*) can improve it [1]. At least in the realm of QRC noise is not to be suppressed in all cases, it could be used as a resource.

In this work we find that a low amplitude damping noise combined with a paradigmatic example of universal gate sets induces a faster approach to Haar-like behavior than when just considering the noiseless case. In order to explain this behaviour, we propose an effective geometric mechanism by which non-unital noise generates a dispersive dynamics on the pure states projective manifold. We develop intuition by means of a one qubit model.

The route to this finding and its explanation is organized as follows. In **Section II** we introduce the amplitude damping channel and define a two-step procedure (noise + renormalization) that induces an effective nonlinear map F_γ on the Bloch sphere. In **Section III** we characterize expansive and contractive regions. In **Section IV**, by means of the well established majorization criterion [20, 21] we show that the approach to Haar-like statistics in a noisy random $G3 = \{H, T, \text{CNOT}\}$ circuit is faster than in the noiseless one. Finally, in **Section V** we discuss the implications of these results and summarize the main conclusions.

II. EFFECTIVE ACTION OF NOISE ON THE BLOCH SPHERE

A. Amplitude damping for one qubit

In noisy quantum systems states are generally a mixed ρ . The state space of a qubit can be conveniently represented through the Bloch decomposition of the density

* jmontes.3@alumni.unav.es

† f.borondo@uam.es

‡ g.carlo@conicet.gov.ar

matrix

$$\rho = \frac{1}{2} (\mathbb{I} + \mathbf{r} \cdot \boldsymbol{\sigma}), \quad (1)$$

where $\boldsymbol{\sigma} = (\sigma_x, \sigma_y, \sigma_z)$ denotes the vector of Pauli matrices and $\mathbf{r} \in \mathbb{R}^3$ is the Bloch vector.

For pure states one has $\text{Tr}(\rho^2) = 1$, which is equivalent to $\|\mathbf{r}\| = 1$; therefore, pure states form the surface of the Bloch sphere, S^2 . A standard parametrization of \mathbf{r} in angular coordinates is

$$\mathbf{r}(\theta, \phi) = \begin{pmatrix} \sin \theta \cos \phi \\ \sin \theta \sin \phi \\ \cos \theta \end{pmatrix}, \quad 0 \leq \theta \leq \pi, \quad 0 \leq \phi < 2\pi, \quad (2)$$

where θ is the polar angle (measured from the north pole, associated with the ground state $|0\rangle$) and ϕ is the azimuthal angle. The area element of the sphere is given by

$$dA = \sin \theta \, d\theta \, d\phi, \quad (3)$$

and it will later define the local expansion/contraction factor of the map induced by noise and renormalization.

We consider the amplitude damping (AD) channel, which models the relaxation $|1\rangle \rightarrow |0\rangle$ with probability $\gamma \in [0, 1]$. In Kraus representation the channel reads

$$\mathcal{E}_\gamma(\rho) = \sum_{k=0,1} E_k \rho E_k^\dagger, \quad (4)$$

with operators

$$E_0 = \begin{pmatrix} 1 & 0 \\ 0 & \sqrt{1-\gamma} \end{pmatrix}, \quad E_1 = \begin{pmatrix} 0 & \sqrt{\gamma} \\ 0 & 0 \end{pmatrix}. \quad (5)$$

This channel is non-unital (in general $\mathcal{E}_\gamma(\mathbb{I}) \neq \mathbb{I}$), reflecting the directionality of the dissipative process towards the ground state. This property is key to generating an effective dynamics on the states of the system.

In terms of the Bloch vector, the AD channel acts affinely on the Bloch sphere. If $\mathbf{r} = (x, y, z)$ corresponds to ρ in (1), then the state $\rho' = \mathcal{E}_\gamma(\rho)$ has Bloch vector $\mathbf{r}' = (x', y', z')$ given by

$$x' = \sqrt{1-\gamma} x, \quad y' = \sqrt{1-\gamma} y, \quad z' = (1-\gamma) z + \gamma. \quad (6)$$

AD contracts all components (x, y, z) (inhomogeneously) but also introduces a translation in z , shifting the distribution of states toward the north pole. In particular, an initial pure state ($\|\mathbf{r}\| = 1$) is mapped in general to a mixed state with $\|\mathbf{r}'\| < 1$.

A simple measure of the mixing induced by the channel can be obtained from the purity. For a qubit,

$$\text{Tr}(\rho'^2) = \frac{1 + \|\mathbf{r}'\|^2}{2}, \quad (7)$$

so that the length $\|\mathbf{r}'\|$ directly quantifies the loss of purity.

B. Dynamics of the principal state: renormalization map

When the mixing is small and the Bloch vector satisfies $\|\mathbf{r}\| \approx 1$, with very high probability our measurements will be effectively equivalent to measuring the pure state with $\|\mathbf{r}\| = 1$, known as the principal state. With the evolution the accumulated noise makes this approximation quickly invalid. But it is still useful in order to understand the step by step process by which non-unital noise contributes to disperse the originally pure state vectors. For this reason we introduce the normalization of our Bloch vector. Also, in the general analysis we relax the restriction of weak noise for completeness.

We start from a pure one-qubit state, represented by a point on the Bloch sphere ($\|\mathbf{r}\| = 1$). As mentioned, after the action of the amplitude damping channel, the state generally becomes mixed and its Bloch vector \mathbf{r}' lies in the interior of the sphere ($\|\mathbf{r}'\| < 1$). In order to identify a geometric mechanism of effective dispersion over the set of pure (principal) states, we introduce the following two-step map:

1. Apply the AD channel, $\rho \mapsto \rho' = \mathcal{E}_\gamma(\rho)$, equivalently $\mathbf{r} \mapsto \mathbf{r}'$ via (6).
2. Associate to ρ' an effective pure state by radial projection onto the surface,

$$\mathbf{r}'' = \frac{\mathbf{r}'}{\|\mathbf{r}'\|}. \quad (8)$$

The result is a deterministic nonlinear map on the sphere,

$$F_\gamma : S^2 \rightarrow S^2, \quad \mathbf{r} \mapsto \mathbf{r}'' = \frac{\mathbf{r}'}{\|\mathbf{r}'\|}, \quad (9)$$

see Fig. 1.

C. Deformation of the Bloch sphere

The AD channel by itself acts linearly on the convex set of states (the Bloch ball), and can be understood as an anisotropic contraction in (x, y, z) combined with a translation in z [22]. However, to describe when and where dissipative noise can increase the dispersion of an ensemble of initially pure states, it is convenient to separate two conceptually distinct effects: (i) the generation of mixing (loss of purity), and (ii) the directional redistribution of the most representative pure states that emerge from the resulting mixed state.

For a qubit, the radial projection (8) selects the point on the sphere aligned with \mathbf{r}' , i.e., it preserves the direction of the state in Bloch space. This choice has two properties that are relevant for our analysis. On one hand, for weak noise $\gamma \rightarrow 0$ one has $\mathbf{r}' \rightarrow \mathbf{r}$ and therefore $\mathbf{r}'' \rightarrow \mathbf{r}$, so that F_γ tends to the identity on S^2 . On the other, the mixing induced by the channel is encoded in

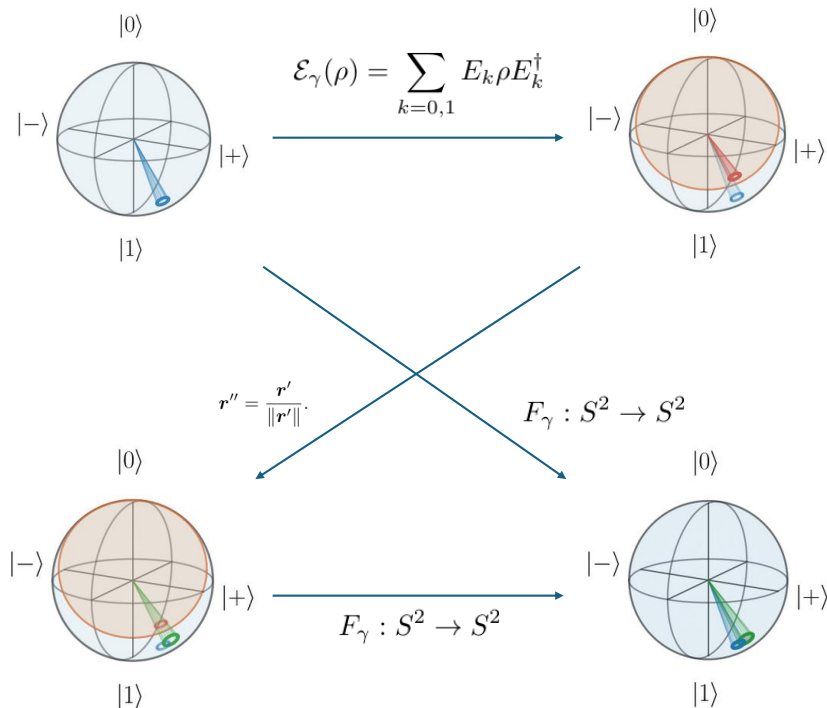


FIG. 1: Schematic representation of the two-step effective map on the Bloch sphere. Starting from a set of pure states (Bloch vectors $\mathbf{r} \in S^2$), shown in blue, we apply the amplitude damping channel $\mathcal{E}_\gamma(\rho) = \sum_{k=0,1} E_k \rho E_k^\dagger$, which maps the states into the interior of the sphere \mathbf{r}' , shown in red. Next, we perform the radial projection $\mathbf{r}'' = \mathbf{r}' / \|\mathbf{r}'\|$, obtaining a set of effective pure states, shown in green. The composition defines the net nonlinear map $F_\gamma : S^2 \rightarrow S^2$.

the norm $N(\theta) = \|\mathbf{r}'\|$, while the degree of dispersion on the sphere depends on the normalized direction \mathbf{r}'' . This allows for an easy comparison between the two effects. F_γ acts as an effective geometric map that captures the tendency of noise to deform and redistribute a set of pure states when one focuses on their directional component.

We apply (6) to the pure state (2). Defining $A := 1 - \gamma$, we obtain

$$\mathbf{r}'(\theta, \phi) = \begin{pmatrix} \sqrt{A} \sin \theta \cos \phi \\ \sqrt{A} \sin \theta \sin \phi \\ A \cos \theta + \gamma \end{pmatrix}, \quad (10)$$

The intermediate norm $N(\theta) = \|\mathbf{r}'\|$ is

$$\begin{aligned} N(\theta)^2 &= A \sin^2 \theta + (A \cos \theta + \gamma)^2 \\ &= 1 - \gamma(1 - \gamma)(1 - \cos \theta)^2, \end{aligned} \quad (11)$$

and therefore

$$N(\theta) = \sqrt{1 - \gamma(1 - \gamma)(1 - \cos \theta)^2}. \quad (12)$$

After the radial projection (8), the direction in the xy plane is preserved, so the azimuthal angle does not change,

$$\phi' = \phi, \quad (13)$$

while the polar angle θ' is determined by the z component of the normalized vector \mathbf{r}'' ,

$$\cos \theta' = \frac{A \cos \theta + \gamma}{N(\theta)} = \frac{(1 - \gamma) \cos \theta + \gamma}{\sqrt{1 - \gamma(1 - \gamma)(1 - \cos \theta)^2}}. \quad (14)$$

Consequently, the map F_γ is axially symmetric and its dynamics reduces to a one-dimensional transformation $\theta \mapsto \theta'(\theta)$, with ϕ as a passive coordinate.

From Eq. (14) becomes clear that the affine term $A \cos \theta + \gamma$ shifts the z component towards more positive values (without the renormalization procedure it would contract the whole sphere to the north pole). By reinserting the states into S^2 , local area expansion arises in certain regions since it amounts to mapping lower measure sections to higher measure ones (effectively increases dispersion on S^2 of the corresponding initial distributions). In what follows, we will refer to this effect as geometric dispersion.

III. EXPANSIVE AND CONTRACTIVE REGIONS

The expression for the local area expansion factor $\Lambda(\theta; \gamma)$ is the central ingredient for identifying expansive

and contractive regions of the proposed map. Below we show how it is obtained from the Jacobian of the angular map.

The renormalized map $F_\gamma : S^2 \rightarrow S^2$ is given by $\phi' = \phi$ and by the relation

$$\begin{aligned} \cos \theta' &= \frac{(1-\gamma)\cos\theta + \gamma}{N(\theta)}, \\ N(\theta) &= \sqrt{1-\gamma(1-\gamma)(1-\cos\theta)^2}. \end{aligned} \quad (15)$$

As a consequence, the Jacobian in coordinates (θ, ϕ) has a diagonal structure,

$$J(\theta, \phi) = \frac{\partial(\theta', \phi')}{\partial(\theta, \phi)} = \begin{pmatrix} \frac{d\theta'}{d\theta} & 0 \\ 0 & 1 \end{pmatrix}, \quad \det J(\theta) = \frac{d\theta'}{d\theta}. \quad (16)$$

The area element on the sphere transforms as $dA' = \sin\theta' d\theta' d\phi'$ and $dA = \sin\theta d\theta d\phi$. Therefore, the local area expansion factor is defined as

$$\Lambda(\theta; \gamma) := \frac{dA'}{dA} = \frac{\sin\theta'}{\sin\theta} \left| \frac{d\theta'}{d\theta} \right|. \quad (17)$$

To evaluate (17) explicitly, we first observe that the transverse component of the Bloch vector after AD satisfies

$$x'^2 + y'^2 = (1-\gamma)\sin^2\theta, \quad (18)$$

while after the radial renormalization $\mathbf{r}'' = \mathbf{r}'/N(\theta)$ one has

$$\sin\theta' = \sqrt{(x'')^2 + (y'')^2} = \frac{\sqrt{x'^2 + y'^2}}{N(\theta)} = \frac{\sqrt{1-\gamma}\sin\theta}{N(\theta)}. \quad (19)$$

Equation (19) immediately yields

$$\frac{\sin\theta'}{\sin\theta} = \frac{\sqrt{1-\gamma}}{N(\theta)}. \quad (20)$$

The direct calculation of $d\theta'/d\theta$ from (15) is algebraically nontrivial; for completeness, the detailed derivation is presented in Appendix A. The result can be written in compact form as

$$\frac{d\theta'}{d\theta} = \sqrt{1-\gamma} \frac{1-\gamma(1-\cos\theta)}{N(\theta)^2}, \quad (21)$$

where the sign is determined by the orientation of the map (in our area analysis we will use the absolute value).

Substituting (20) and (21) into (17) finally gives

$$\Lambda(\theta; \gamma) = (1-\gamma) \frac{|1-\gamma(1-\cos\theta)|}{[1-\gamma(1-\gamma)(1-\cos\theta)^2]^{3/2}}, \quad (22)$$

where we used $N(\theta)^2 = 1-\gamma(1-\gamma)(1-\cos\theta)^2$. The condition $\Lambda(\theta; \gamma) > 1$ identifies a locally expansive region, while $\Lambda(\theta; \gamma) < 1$ corresponds to local area contraction.

We therefore define the boundary $\theta_c(\gamma) \in (0, \pi)$ as the value (when it exists) satisfying

$$\Lambda(\theta_c(\gamma); \gamma) = 1, \quad (23)$$

so that the regions $\theta < \theta_c(\gamma)$ and $\theta > \theta_c(\gamma)$ correspond, respectively, to local contraction and local area expansion. Equivalently, the expansive set for a given γ is

$$\mathcal{E}_\gamma = \{(\theta, \phi) \in S^2 : \Lambda(\theta; \gamma) > 1\} = \{(\theta, \phi) : \theta \in (\theta_c(\gamma), \pi)\}, \quad (24)$$

provided the solution $\theta_c(\gamma)$ exists. In what follows we will refer to the region $\theta \approx \pi$ as the *neighborhood of the south pole* (states with larger excited-state population), and to $\theta \approx 0$ as the *neighborhood of the north pole* (the ground state).

A first asymptotic analysis is in order here. We see the behavior of Λ at the poles. Using (22):

North pole ($\theta = 0$). Since $1 - \cos\theta = 0$ and $\theta' = \theta$ at the north pole, we obtain

$$\Lambda(0; \gamma) = 1 - \gamma. \quad (25)$$

Therefore, for any $\gamma > 0$ the map is contractive in a neighborhood of the north pole.

South pole ($\theta = \pi$). Since $1 - \cos\pi = 2$, the denominator of (22) simplifies via $1 - 4\gamma(1-\gamma) = (1-2\gamma)^2$, and we obtain

$$\Lambda(\pi; \gamma) = \frac{1-\gamma}{|1-2\gamma|^2}. \quad (26)$$

This expression exhibits a singular behavior as $\gamma \rightarrow 1/2$, associated with the fact that the intermediate mixed state collapses to $\mathbf{r}' = \mathbf{0}$ when starting from the south pole with $\gamma = 1/2$, making the radial projection (8) ill-defined at that isolated point. On the rest of the sphere, and for $\gamma \neq 1/2$, the map remains well defined.

Equations (25)–(26) capture the essential asymmetry of the map: while the north pole is always contractive for $\gamma > 0$, the south pole can be strongly expansive for certain values of γ .

The expansive set \mathcal{E}_γ exists if and only if $\Lambda(\theta; \gamma)$ exceeds the threshold 1 for some $\theta \in (0, \pi)$. Since for $\gamma \rightarrow 1$ the expansion reduces to the neighborhood of the south pole, a necessary and sufficient condition is

$$\Lambda(\pi; \gamma) > 1. \quad (27)$$

Using (26), the inequality $\Lambda(\pi; \gamma) > 1$ is equivalent to

$$\frac{1-\gamma}{|1-2\gamma|^2} > 1 \iff \gamma(3-4\gamma) > 0. \quad (28)$$

Therefore, for $\gamma \in (0, 1)$ one obtains the global threshold

$$0 < \gamma < \frac{3}{4} \iff \exists \theta : \Lambda(\theta; \gamma) > 1, \quad (29)$$

whereas

$$\gamma \geq \frac{3}{4} \implies \Lambda(\theta; \gamma) \leq 1 \quad \forall \theta \in [0, \pi]. \quad (30)$$

In other words: for sufficiently strong noise ($\gamma \geq 3/4$) the renormalized dynamics is globally area-contracting, whereas for low to intermediate noise ($0 < \gamma < 3/4$) an expansive belt emerges around the south pole.

Figure 2 illustrates how the renormalized map produces a trade-off between geometric dispersion and mixing. For low to intermediate values of γ (panels a–d: $\gamma = 0.01, 0.1, 0.2, 0.45$) we apply the map F_γ and plot the local area expansion factor $\Lambda(\theta; \gamma)$ together with the expansive region (where $\Lambda > 1$). When γ is small ($\gamma = 0.01$), the expansive region is maximal in angular extent, but the expansion is very weak, with $\Lambda(\theta)$ barely above unity. For $\gamma = 0.1$ the expansive region remains large and the magnitude of the expansion increases appreciably (typical values around $\Lambda \simeq 1.4$). Increasing to $\gamma = 0.2$, the expansive area shrinks, but the local expansion grows strongly; however, as shown in the *inset*, the degree of mixing is already significant (loss of purity associated with $N(\theta) = \|\mathbf{r}'\|$). Finally, for $\gamma = 0.45$ the expansion is large but becomes confined to a very small neighborhood of the south pole, and the purity is low.

For $\gamma \in (0, 3/4)$, Eq. (23) defines a boundary $\theta_c(\gamma)$ separating the contractive region (near the north pole) from the expansive region (near the south pole). Although $\theta_c(\gamma)$ does not in general admit a simple closed form, it is obtained directly as the one-dimensional solution of $\Lambda(\theta; \gamma) = 1$ and can be numerically calculated.

The local analysis in terms of $\Lambda(\theta; \gamma)$ identifies which regions of the sphere are expansive or contractive. Though we are interested in the very weak noise limit, it is interesting to visualize the general behaviour of the renormalization map. Figure 3 provides a global idea of the expansion/contraction induced by F_γ on S^2 in terms of $\log(\Lambda)$. Consistently with Fig. 2, for $\gamma = 0.01$ (panel a) the expansive region appears as a broad belt around the south pole, but with very weak intensity (values of $\log(\Lambda)$ close to zero). Moving to $\gamma = 0.1$ (panel b) the expansive area remains extensive and the intensity increases appreciably. For $\gamma = 0.2$ (panel c) the red zone becomes more concentrated near the south pole: the expansive area decreases, although the local expansion is stronger. Finally, for $\gamma = 0.45$ (panel d) the extreme expansion is confined to a very small neighborhood of the south pole, with the rest of the sphere dominated by contraction, reflecting the trade-off between expansion intensity and angular extent of the expansive region.

IV. NOISE ACCELERATES APPROACH TO HAAR-LIKE BEHAVIOUR

In the previous sections we used a geometric analysis to show that the same noise channel that generates mixing induces an effective dispersion on the pure-state projective manifold. Here we connect this mechanism with a standard benchmark of random-circuit complexity: the majorization criterion of [20, 21]. We must underline that our aim is not measuring how noise spoils the

quality of a Haar operators ensemble like for example in t-design studies [23]. On the contrary, we are interested in showing how relatively weak noise can lead to an initially faster effective exploration of it. For this purpose the majorization criterion is suitable.

If we have an n -qubit pure state $|\psi\rangle \in \mathbb{C}^d$ with $d = 2^n$, we consider computational-basis measurement probabilities

$$P(i) = |\psi_i|^2, \quad i = 1, \dots, d. \quad (31)$$

For a mixed state ρ we consider the main diagonal as the probability vector $P(i)$. Let P^\downarrow be the sorted vector in descending order, $P^\downarrow(1) \geq \dots \geq P^\downarrow(d)$, and define the cumulative sums (cumulants)

$$C(k) = \sum_{j=1}^k P^\downarrow(j), \quad k = 1, \dots, d. \quad (32)$$

Given an ensemble of M states at a given depth t , we define the SDL signature as the sample standard deviation of the cumulants across the ensemble,

$$\text{SDL}(k; t) = \sqrt{\mathbb{E}_m [C_t^{(m)}(k)^2] - \left(\mathbb{E}_m [C_t^{(m)}(k)]\right)^2}. \quad (33)$$

We then define a scalar distance to Haar by comparing with a Haar reference SDL_{Haar} (estimated from M_{Haar} Haar states in dimension d):

$$D(t) = \|\text{SDL}(t) - \text{SDL}_{\text{Haar}}\|_2. \quad (34)$$

This is the majorization criterion which provides with a compact and efficient diagnostics of Haar-likeness for ensembles, including weak noise scenarios.

We consider random circuits built from the universal gate set $G3 = \{H, T, \text{CNOT}\}$. At each layer, a single gate is drawn with probabilities

$$\mathbb{P}(H) = \mathbb{P}(T) = \mathbb{P}(\text{CNOT}) = \frac{1}{3}, \quad (35)$$

where H or T acts on a uniformly random qubit, and CNOT acts on a uniformly random ordered pair of distinct qubits. Starting from $|0\rangle^{\otimes n}$ for instance, we propagate an ensemble of M samples up to depth T and evaluate $D(t)$ at each depth.

We compare two evolutions, the pure state evolution under the random unitary circuit $|\psi\rangle \mapsto U|\psi\rangle$ and the noisy one (along each unitary gate we apply local amplitude damping on the idle qubits – we assume perfect gates – with uniform γ values). To reduce Monte Carlo variance in the comparison the same random gate realization is applied in both cases (unitary and noisy). This allows to better see the amplitude damping induced geometric dispersion contribution. We have considered the following simulation parameters: $M = 3000$, $M_{\text{Haar}} = 3000$, depths up to $T = 200, 220$, and $n = 6, 7$ qubits.

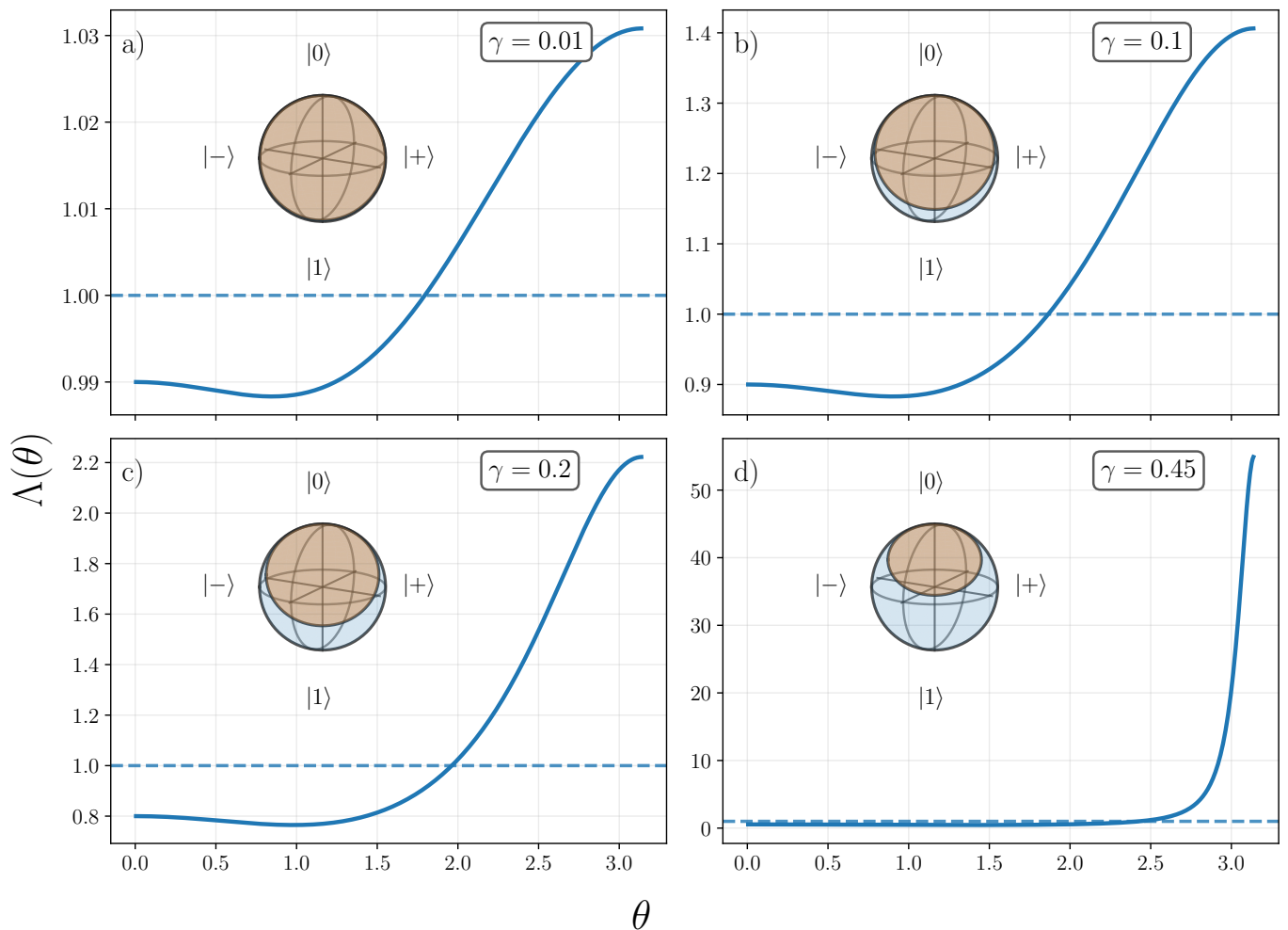


FIG. 2: Local area expansion factor $\Lambda(\theta; \gamma)$ of the map F_γ as a function of the polar angle θ . Panels (a)–(d) correspond to $\gamma = 0.01, 0.1, 0.2$ and 0.45 , respectively. The dashed line marks the threshold $\Lambda = 1$ separating contractive regions ($\Lambda < 1$) from expansive regions ($\Lambda > 1$). *Inset*: Bloch-sphere representation of the effect of the amplitude damping channel prior to renormalization: the outer sphere corresponds to the set of initial pure states ($\|\mathbf{r}\| = 1$), while the inner sphere shows the image under AD, $\mathbf{r} \mapsto \mathbf{r}'$.

For $n = 6$, we find that the distance to Haar of the diagonal of the density matrix ρ' for SDL(t) in Figure 4(a) reduces faster with noise than with purely unitary dynamics. For weak noise ($\gamma = 0.001$), at around 150 gates the distance to Haar is similar to that of 200 noiseless gates. Stronger noise ultimately introduces a bias that limits asymptotic proximity to Haar. This prevents from an exact coincidence of the cumulant fluctuations with those of Haar. In any case, we underline that the distance $D(t)$ decreases more rapidly than in the purely unitary case over an extended range of depths. Operationally, this means that at a fixed finite depth – a relevant regime in NISQ and reservoir-like settings – the noisy ensemble can be closer to Haar sooner.

The same behaviour is observed when considering $n = 7$ qubits. Now, at around 180 gates the distance to Haar is similar to that of 220 noiseless gates. This can be seen in Figure 4(b).

This behavior is naturally understood thanks to our geometric analysis. The non unitary channel effective map on the projective manifold of pure states introduces a directional deformation towards regions of greater measure, globally. In the weak noise regime, this induced expansion contributes an additional effective dispersion of states that can enhance the quantum randomness of measurement probabilities at finite depth, thereby reducing $D(t)$ faster. This is further confirmed by looking at Fig. 5 where we have repeated the same simulations leading to Fig. 4 but initializing the quantum state at $|1\rangle^{\otimes n}$. The approach to Haar like behavior is even faster. In fact, this initial state is in the maximal expansion region of each qubit (see Fig. 3).

Regarding limitations of this mechanism, these results are in line with the analysis of the previous Sections. As γ increases, dissipation becomes dominant and introduces a progressively stronger bias toward the computational

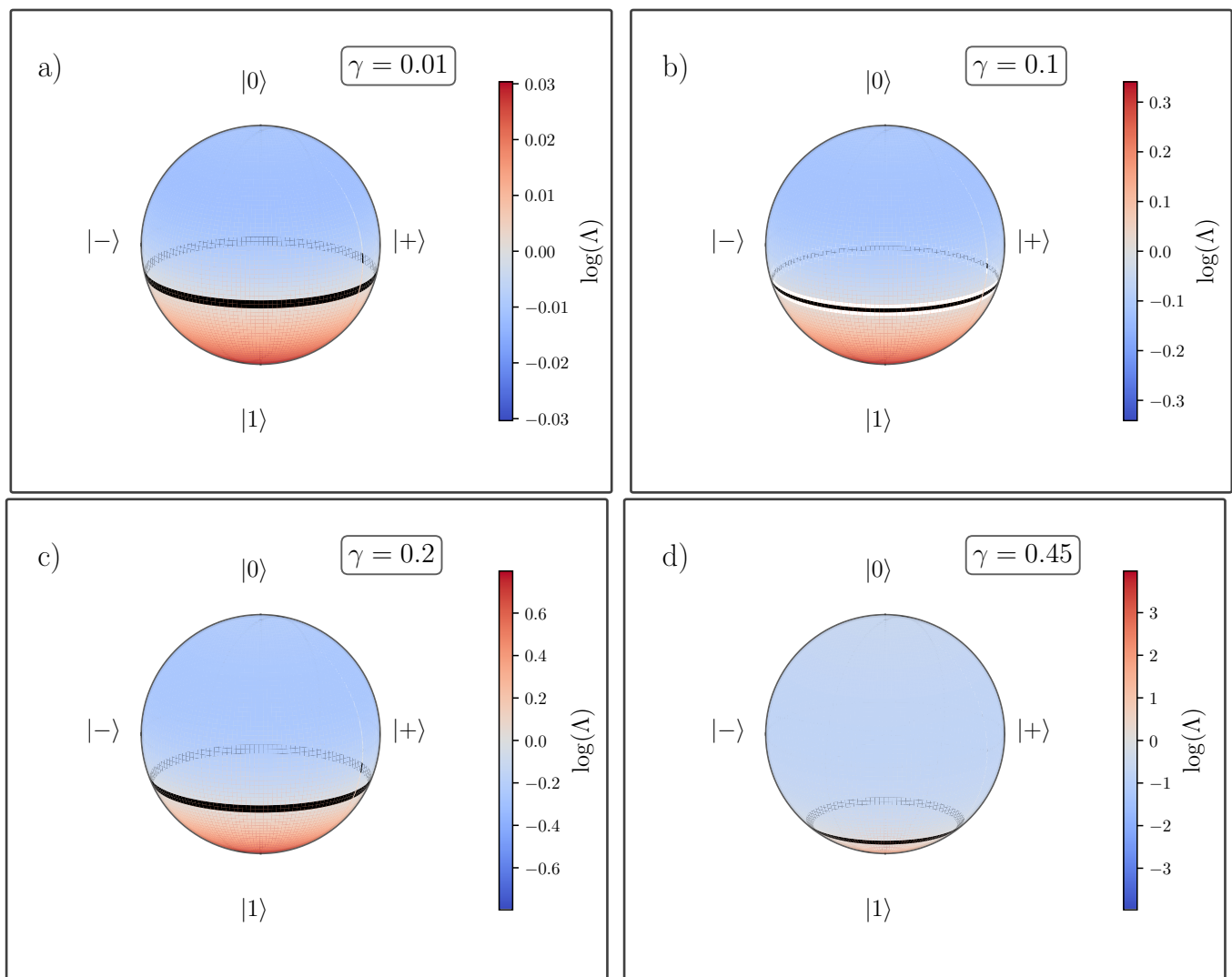


FIG. 3: Map of the local area expansion factor over the Bloch sphere, represented as $\log(\Lambda(\theta; \gamma))$. Blue tones indicate contractive regions ($\Lambda < 1$) and red tones expansive regions ($\Lambda > 1$). The black curve marks the boundary $\Lambda(\theta_c(\gamma); \gamma) = 1$ that separates both dynamics. Panels (a)–(d) correspond to $\gamma = 0.01, 0.1, 0.2$ and 0.45 , respectively.

zero state. While this can produce a rapid initial decay, it also leads to a restriction with respect to asymptotic relaxation to Haar: for sufficiently large γ and/or gate number, the distance $D(t)$ does not continue decreasing as in the unitary dynamics. Moreover, the approximation to truly Haar-like fluctuations is limited. Non-unital noise provides a finite-depth speedup toward Haar-like statistics, but excessive (eventually accumulated) noise ultimately prevents arbitrarily close convergence by injecting a preferred direction in state space.

V. CONCLUSIONS

In this work we have shown that non-unital noise can be interpreted as a generator of an effective dynamics when its action is viewed through the dominant pure-

state. For the minimal one-qubit case, the composition of amplitude damping with renormalization induces a non-linear map F_γ on S^2 whose geometry is quantified by the local factor $\Lambda(\theta; \gamma)$. This analysis reveals a sharp separation between contractive zones (near the north pole) and an expansive belt (near the south pole) that exists only for $0 < \gamma < 3/4$. When combined with random circuits drawn from a paradigmatic universal gate set like G3 the global effect is an enhanced Haar convergence due to induced geometric dispersion.

We can explain this remarkable result by means of our geometrical analysis of the projection on pure principal states. These findings complement previous observations in quantum reservoir computing where noise acts as a resource under controlled conditions. Hence, we open the chance to extended the applicability of noise as a resource for quantum computational algorithms in general. We

hope that our point of view will contribute to more uses of available NISQ technology.

-
- [1] L. Domingo, F. Borondo, and G. G. Carlo. Taking advantage of noise in quantum reservoir computing. *Scientific Reports*, 13:8790, 2023.
- [2] Frank Arute, Kunal Arya, Ryan Babbush, et al. Quantum supremacy using a programmable superconducting processor. *Nature*, 574:505–510, 2019.
- [3] Han-Sen Zhong, Li-Chao Peng, Yuan Li, Yi Hu, Wei Li, Jian Qin, Dian Wu, Weijun Zhang, Hao Li, Lu Zhang, Zhen Wang, Lixing You, Xiao Jiang, Li Li, Nai-Le Liu, Jonathan P. Dowling, Chao-Yang Lu, and Jian-Wei Pan. Experimental Gaussian boson sampling. *Science Bulletin*, 64(8):511–515, 2019.
- [4] Aram W. Harrow and Ashley Montanaro. Quantum computational supremacy. *Nature*, 549:203–209, 2017.
- [5] Adrian Cho. Ibm casts doubt on Google’s claims of quantum supremacy. Science.org, 2019. Accessed: 2026-02-12.
- [6] Yong (Alexander) Liu, Xin (Lucy) Liu, Fang (Nancy) Li, Haohuan Fu, Yuling Yang, Jiawei Song, Pengpeng Zhao, Zhen Wang, Dajia Peng, Huarong Chen, Chu Guo, Heliang Huang, Wenzhao Wu, and Dexun Chen. Closing the “quantum supremacy” gap: Achieving real-time simulation of a random quantum circuit using a new sunway supercomputer. In *Proceedings of the International Conference for High Performance Computing, Networking, Storage and Analysis (SC ’21)*. Association for Computing Machinery, 2021.
- [7] Y. Zhao et al. Realization of an error-correcting surface code with superconducting qubits. *Phys. Rev. Lett.*, 129:030501, 2022.
- [8] Chibueze Ugwuishiwu, O. Ugochukwu, O. Ukwueze, and P. Ogbobe. A review on the fundamental concepts of quantum elements, efficient quantum algorithms and quantum error correcting codes. *International Journal of Scientific & Technology Research*, 11:1–, 2022.
- [9] Ryuji Takagi, Suguru Endo, Shintaro Minagawa, and Mile Gu. Fundamental limits of quantum error mitigation. *npj Quantum Information*, 8:114, 2022.
- [10] Yong Guo and Shengyu Yang. Quantum error mitigation via matrix product operators. *PRX Quantum*, 3:040313, 2022.
- [11] Rajeev Acharya et al. Suppressing quantum errors by scaling a surface code logical qubit. *Nature*, 614:676–681, 2023.
- [12] P. Mujal et al. Opportunities in quantum reservoir computing and extreme learning machines. *Advanced Quantum Technologies*, 4:2100027, 2021.
- [13] Keisuke Fujii and Kouhei Nakajima. Harnessing disordered-ensemble quantum dynamics for machine learning. *Phys. Rev. Applied*, 8:024030, 2017.
- [14] Kouhei Nakajima, Keisuke Fujii, Makoto Negoro, Kosuke Mitarai, and Masahiro Kitagawa. Boosting computational power through spatial multiplexing in quantum reservoir computing. *Phys. Rev. Applied*, 11:034021, 2019.
- [15] A. Kutvonen, K. Fujii, and T. Sagawa. Optimizing a quantum reservoir computer for time series prediction. *Scientific Reports*, 10:14687, 2020.
- [16] J. Chen, H. I. Nurdin, and N. Yamamoto. Temporal information processing on noisy quantum computers. *Phys. Rev. Applied*, 14:024065, 2020.
- [17] R. Martínez-Peña, J. Nokkala, G. L. Giorgi, and J. Amato-Grill. Information processing capacity of spin-based quantum reservoir computing systems. *Cognitive Computation*, 2020.
- [18] R. Martínez-Peña, G. L. Giorgi, J. Nokkala, M. C. Soriano, and R. Zambrini. Dynamical phase transitions in quantum reservoir computing. *Phys. Rev. Lett.*, 127:100502, 2021.
- [19] S. Ghosh, A. Opala, M. Matuszewski, T. Paterek, and T. C. H. Liew. Quantum reservoir processing. *npj Quantum Information*, 5:35, 2019.
- [20] Fernando de Melo Raúl O. Vallejos and Gabriel G. Carlo. Principle of majorization: Application to random quantum circuits. *Phys. Rev. A*, 104:012602, 2021.
- [21] Gabriel G. Carlo Fernando de Melo Alexandre B. Tacla, Nina M. O’Neill and Raúl O. Vallejos. Majorization-based benchmark of the complexity of quantum processors. *Quantum Information Processing*, 23:240, 2024.
- [22] Michael A. Nielsen and Isaac L. Chuang. *Quantum Computation and Quantum Information*. Cambridge University Press, Cambridge, UK, 2000.
- [23] Conrad Strydom and Mark Tame. Investigating the effect of noise channels on the quality of unitary t-designs. *Phys. Rev. A*, 108:052414, 2023.

Appendix A: Derivation of $\Lambda(\theta; \gamma)$

Let us consider the vector

$$\mathbf{r}'(\theta, \phi) = \begin{pmatrix} \sqrt{A} \sin \theta \cos \phi \\ \sqrt{A} \sin \theta \sin \phi \\ A \cos \theta + \gamma \end{pmatrix}, \quad (\text{A1})$$

and define

$$N(\theta) := \|\mathbf{r}'(\theta, \phi)\|. \quad (\text{A2})$$

Since $N(\theta)$ is the Euclidean norm, we have

$$\begin{aligned} N(\theta)^2 &= \left(\sqrt{A} \sin \theta \cos \phi\right)^2 + \left(\sqrt{A} \sin \theta \sin \phi\right)^2 + (A \cos \theta + \gamma)^2 \\ &= A \sin^2 \theta (\cos^2 \phi + \sin^2 \phi) + (A \cos \theta + \gamma)^2 \\ &= A \sin^2 \theta + (A \cos \theta + \gamma)^2. \end{aligned} \quad (\text{A3})$$

The angular map is given by

$$\cos \theta' = \frac{A \cos \theta + \gamma}{N(\theta)}, \quad \phi' = \phi, \quad (\text{A4})$$

or equivalently,

$$\theta' = \arccos\left(\frac{A \cos \theta + \gamma}{N(\theta)}\right). \quad (\text{A5})$$

1. Jacobian of the map

Since $\phi' = \phi$ and θ' does not depend on ϕ , the Jacobian is triangular:

$$J(\theta, \phi) = \begin{pmatrix} \frac{\partial \theta'}{\partial \theta} & \frac{\partial \theta'}{\partial \phi} \\ \frac{\partial \phi'}{\partial \theta} & \frac{\partial \phi'}{\partial \phi} \end{pmatrix} = \begin{pmatrix} \frac{d\theta'}{d\theta} & 0 \\ 0 & 1 \end{pmatrix}. \quad (\text{A6})$$

Therefore, the only nontrivial term is $d\theta'/d\theta$.

2. Closed-form derivation of $\frac{d\theta'}{d\theta}$

We define

$$p(\theta) := A \cos \theta + \gamma, \quad u(\theta) := \frac{p(\theta)}{N(\theta)}. \quad (\text{A7})$$

Then, by (A4), we have $\cos \theta' = u(\theta)$. Differentiating implicitly with respect to θ :

$$\frac{d}{d\theta} \cos \theta' = -\sin \theta' \frac{d\theta'}{d\theta} = \frac{du}{d\theta}. \quad (\text{A8})$$

Hence,

$$\frac{d\theta'}{d\theta} = -\frac{u'(\theta)}{\sin \theta'}. \quad (\text{A9})$$

a. (i) Expression of $\sin \theta'$ in terms of θ . Using $\cos \theta' = u$,

$$\begin{aligned} \sin^2 \theta' &= 1 - \cos^2 \theta' = 1 - u(\theta)^2 = 1 - \frac{p(\theta)^2}{N(\theta)^2} \\ &= \frac{N(\theta)^2 - p(\theta)^2}{N(\theta)^2}. \end{aligned} \quad (\text{A10})$$

From (A3) we have $N(\theta)^2 - p(\theta)^2 = A \sin^2 \theta$, hence

$$\sin^2 \theta' = \frac{A \sin^2 \theta}{N(\theta)^2}, \quad \Rightarrow \quad \sin \theta' = \frac{\sqrt{A} \sin \theta}{N(\theta)}. \quad (\text{A11})$$

(For the usual range $0 \leq \theta \leq \pi$ we take $\sin \theta \geq 0$.)

b. (ii) Computation of $u'(\theta)$. Since $u = p/N$, by the quotient rule:

$$u'(\theta) = \frac{p'(\theta)N(\theta) - p(\theta)N'(\theta)}{N(\theta)^2}. \quad (\text{A12})$$

Moreover,

$$p'(\theta) = \frac{d}{d\theta} (A \cos \theta + \gamma) = -A \sin \theta. \quad (\text{A13})$$

Substituting (A12) and (A11) into (A9):

$$\frac{d\theta'}{d\theta} = -\frac{\frac{p'N - pN'}{N^2}}{\frac{\sqrt{A} \sin \theta}{N}} = -\frac{p'N - pN'}{N\sqrt{A} \sin \theta} = \quad (\text{A14})$$

$$-\frac{p'}{\sqrt{A} \sin \theta} + \frac{p}{\sqrt{A} \sin \theta} \frac{N'}{N}. \quad (\text{A15})$$

With (A13) we obtain

$$-\frac{p'}{\sqrt{A} \sin \theta} = -\frac{-A \sin \theta}{\sqrt{A} \sin \theta} = \sqrt{A}, \quad (\text{A16})$$

and therefore

$$\frac{d\theta'}{d\theta} = \sqrt{A} + \frac{p}{\sqrt{A} \sin \theta} \frac{N'}{N}. \quad (\text{A17})$$

c. (iii) Computation of $\frac{N'}{N}$. We differentiate (A3):

$$N(\theta)^2 = A \sin^2 \theta + p(\theta)^2. \quad (\text{A18})$$

Then

$$\begin{aligned} 2NN' &= 2A \sin \theta \cos \theta + 2pp' \\ \Rightarrow \frac{N'}{N} &= \frac{A \sin \theta \cos \theta + pp'}{N^2}. \end{aligned} \quad (\text{A19})$$

Using $p' = -A \sin \theta$ in (A19):

$$\frac{N'}{N} = \frac{A \sin \theta \cos \theta - Ap \sin \theta}{N^2} = \frac{A \sin \theta (\cos \theta - p)}{N^2}. \quad (\text{A20})$$

Substituting (A20) into (A17):

$$\begin{aligned} \frac{d\theta'}{d\theta} &= \sqrt{A} + \frac{p}{\sqrt{A} \sin \theta} \cdot \frac{A \sin \theta (\cos \theta - p)}{N^2} \\ &= \sqrt{A} + \sqrt{A} \frac{p(\cos \theta - p)}{N^2} = \sqrt{A} \left(1 + \frac{p \cos \theta - p^2}{N^2} \right) \\ &= \sqrt{A} \frac{N^2 + p \cos \theta - p^2}{N^2}. \end{aligned} \quad (\text{A21})$$

Using $N^2 = A \sin^2 \theta + p^2$ in the numerator of (A21):

$$\begin{aligned} N^2 + p \cos \theta - p^2 &= A \sin^2 \theta + p^2 + p \cos \theta - p^2 = A \sin^2 \theta + p \cos \theta \\ &= A(1 - \cos^2 \theta) + (A \cos \theta + \gamma) \cos \theta \\ &= A - A \cos^2 \theta + A \cos^2 \theta + \gamma \cos \theta = A + \gamma \cos \theta. \end{aligned} \quad (\text{A22})$$

Therefore,

$$\boxed{\frac{d\theta'}{d\theta} = \sqrt{A} \frac{A + \gamma \cos \theta}{N(\theta)^2}}. \quad (\text{A23})$$

3. Case $A = 1 - \gamma$

In the case used in the main text, $A = 1 - \gamma$. Moreover, from the norm calculation (see (A3) and the corresponding simplification) one has

$$N(\theta)^2 = 1 - \gamma(1 - \gamma)(1 - \cos \theta)^2. \quad (\text{A24})$$

The numerator of (A23) becomes

$$A + \gamma \cos \theta = (1 - \gamma) + \gamma \cos \theta = 1 - \gamma(1 - \cos \theta). \quad (\text{A25})$$

Substituting into (A23) and using (A24):

$$\boxed{\frac{d\theta'}{d\theta} = \sqrt{1-\gamma} \frac{1-\gamma(1-\cos\theta)}{1-\gamma(1-\gamma)(1-\cos\theta)^2}}. \quad (\text{A26})$$

as

$$\boxed{J(\theta, \phi) = \begin{pmatrix} \frac{d\theta'}{d\theta} & 0 \\ 0 & 1 \end{pmatrix}}$$

with $\frac{d\theta'}{d\theta}$ given by (A26).

Finally, the Jacobian of the map (A4) can be written

(A27)

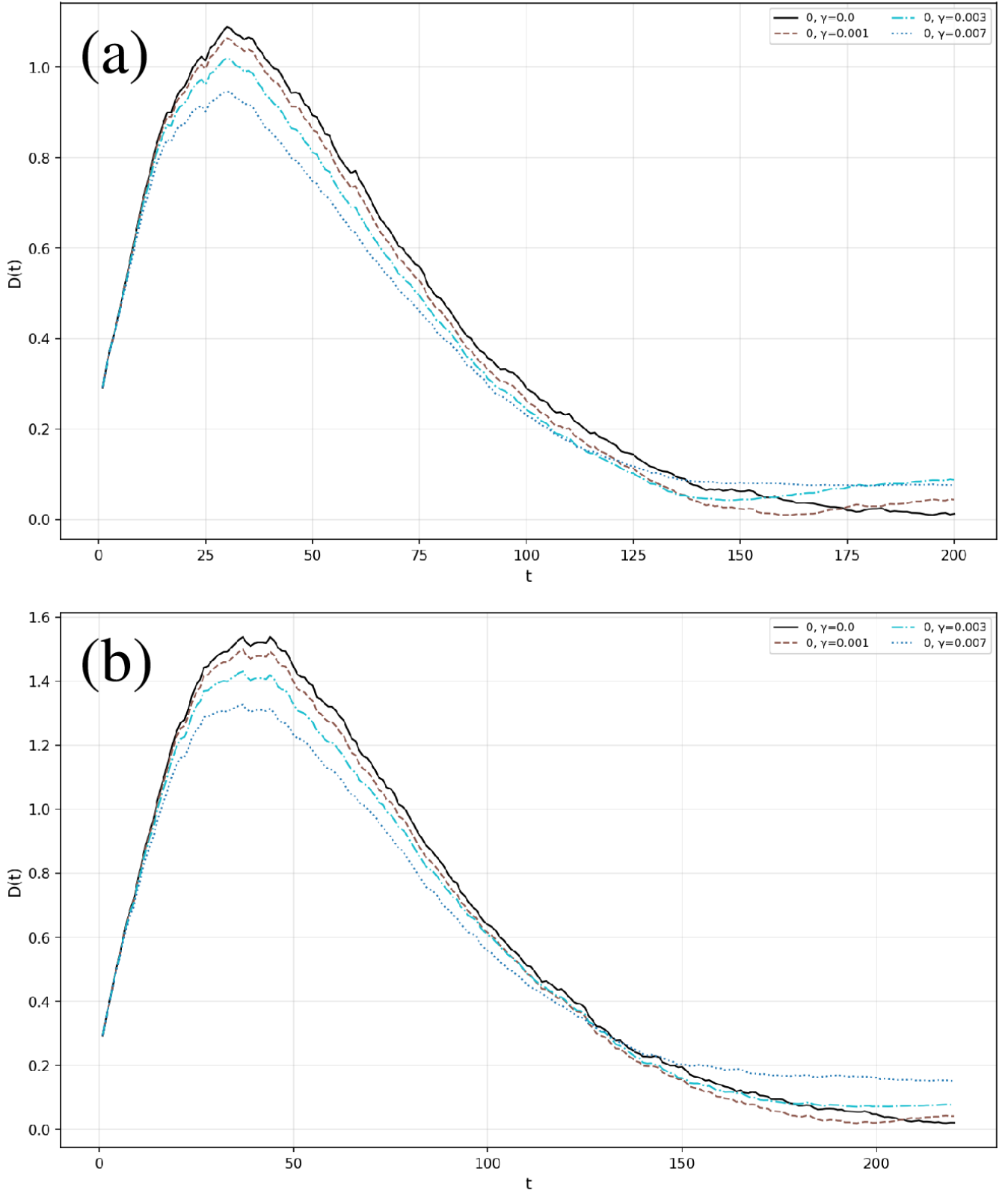


FIG. 4: (a) SDL-distance to Haar, $D(t) = \|\text{SDL}(t) - \text{SDL}_{\text{Haar}}\|_2$, as a function of circuit depth for random G3 circuits of $n = 6$ qubits. Solid black line: unitary G3 evolution. Other patterns and colors indicated in the panel: G3 followed by local amplitude damping with different γ parameters. (b) Same as in panel (a) but for $n = 7$ qubits.

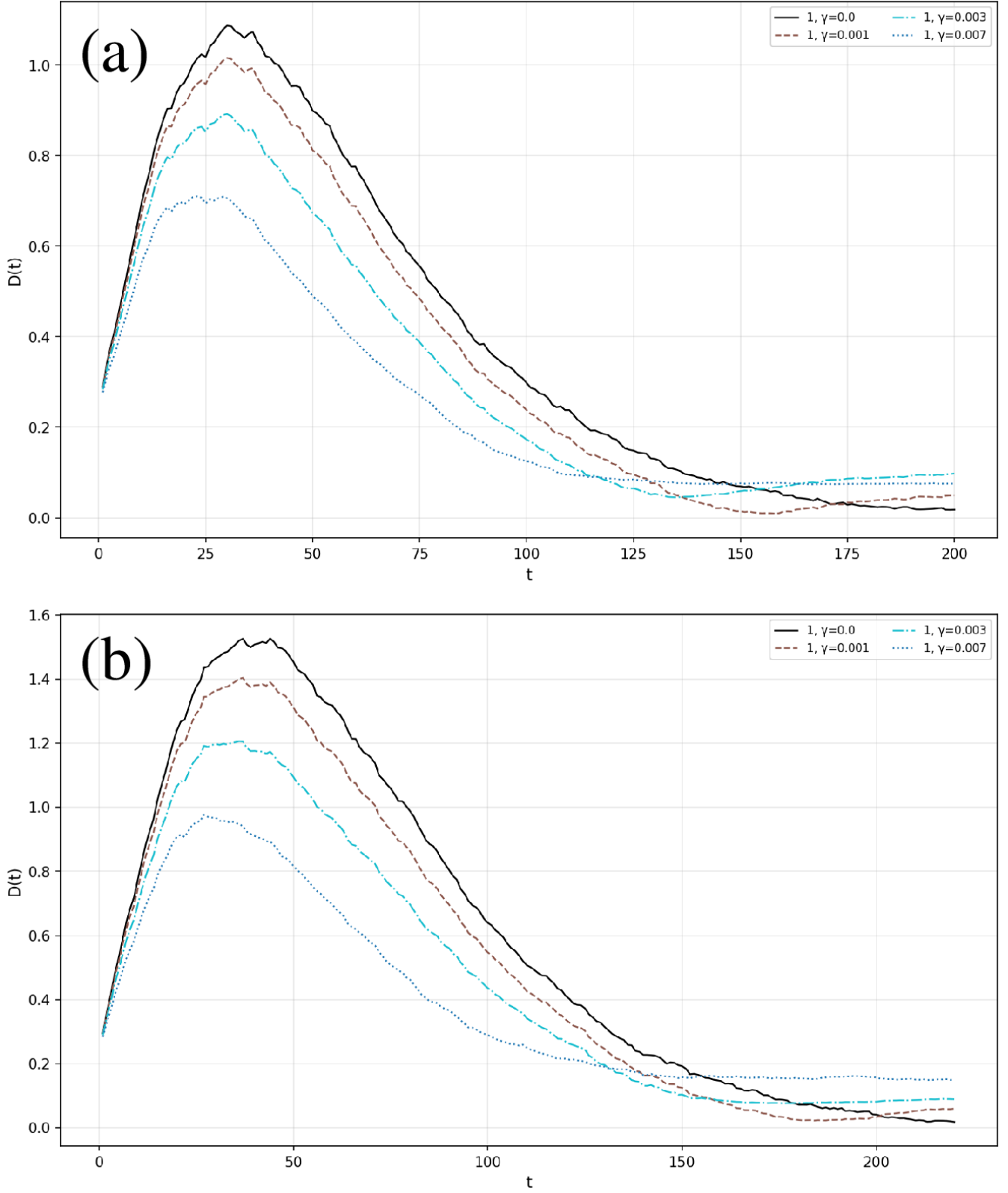


FIG. 5: Same as in Fig. 4, but considering $|1\rangle^{\otimes n}$ as the initial state.